Supporting Information:

Three-Dimensional Morphological and Chemical Evolution of Nanoporous Stainless Steel by Liquid Metal Dealloying

Chonghang Zhao[1], Takeshi Wada[2], Vincent De Andrade[3], Garth J. Williams[4], Jeff Gelb[5], Li Li[4], Juergen Thieme[4], Hidemi Kato[2], Yu-chen Karen Chen-Wiegart[4,1]*

[1] Department of Materials Science and Chemical Engineering, Stony Brook University, Stony Brook, New York, 11794, United States

[2] Institute for Materials Research, Tohoku University, Katahira, Sendai, 980-8577, Japan

[3] Advanced Photon Source, Argonne National Laboratory, Argonne, Illinois, 60439, United States

[4] National Synchrotron Light Source II, Brookhaven National Laboratory, Upton, New York, 11973, United States

[5] ZEISS Group, Carl Zeiss X-Ray Microscopy, Inc., Pleasanton, California, 94588, United States

Email: karen.chen-wiegart@stonybrook.edu

S1. Experimental Setups

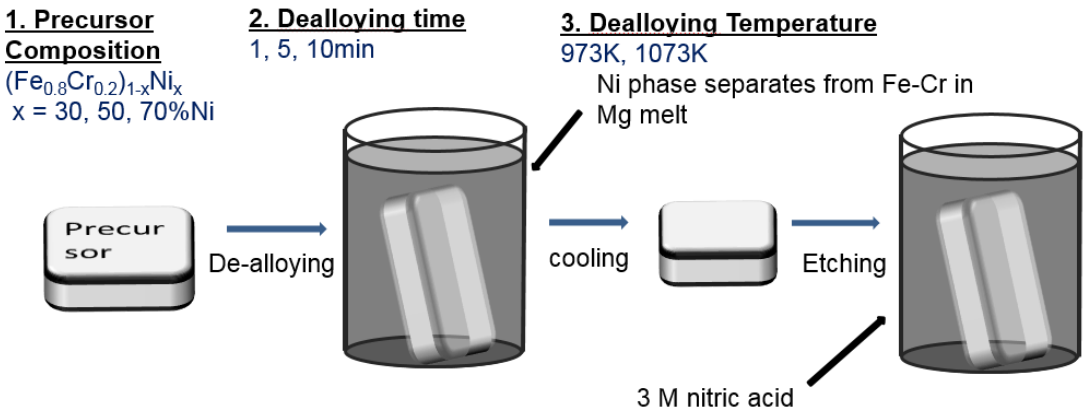

Figure S1. Schematic of dealloying process.

Precursor Compositions / Dealloying Time (min) / Temp. (K)		1	5	10
$(Fe_{0.8}Cr_{0.2})_{30}Ni_{70}$	973	70%Ni-973K-1min	70%Ni-973K-5min	70%Ni-973K-10min
	1073	70%Ni-1073K-1min	70%Ni-1073K-5min	70%Ni-1073K-10min
$(Fe_{0.8}Cr_{0.2})_{50}Ni_{50}$	973	50%Ni-973K-1min	50%Ni-973K-5min	50%Ni-973K-10min
	1073	50%Ni-1073K-1min	50%Ni-1073K-5min	50%Ni-1073K-10min
$(Fe_{0.8}Cr_{0.2})_{70}Ni_{30}$	973	30%Ni-973K-1min	30%Ni-973K-5min	30%Ni-973K-10min

Table S1. All conditions being studied in this work: precursor compositions, dealloying time and temperature

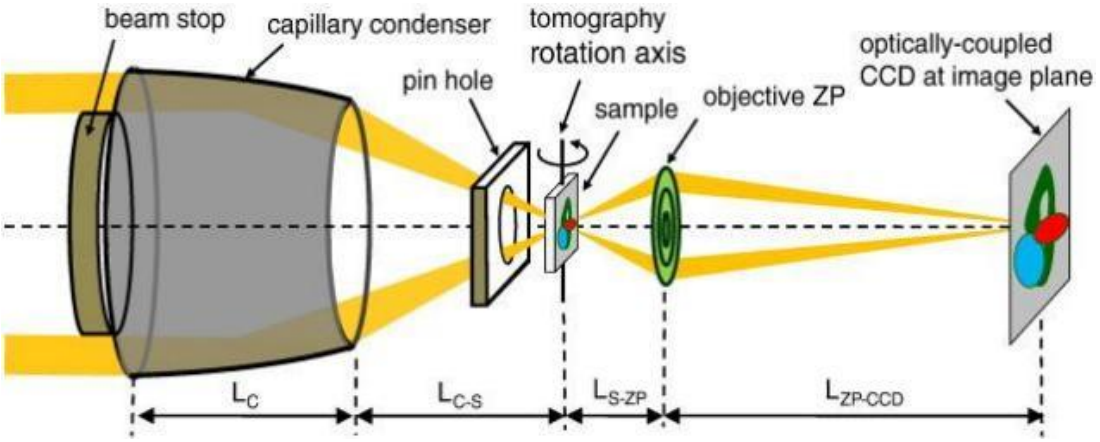

Figure S2. Schematics of x-ray nano-tomography experimental setup

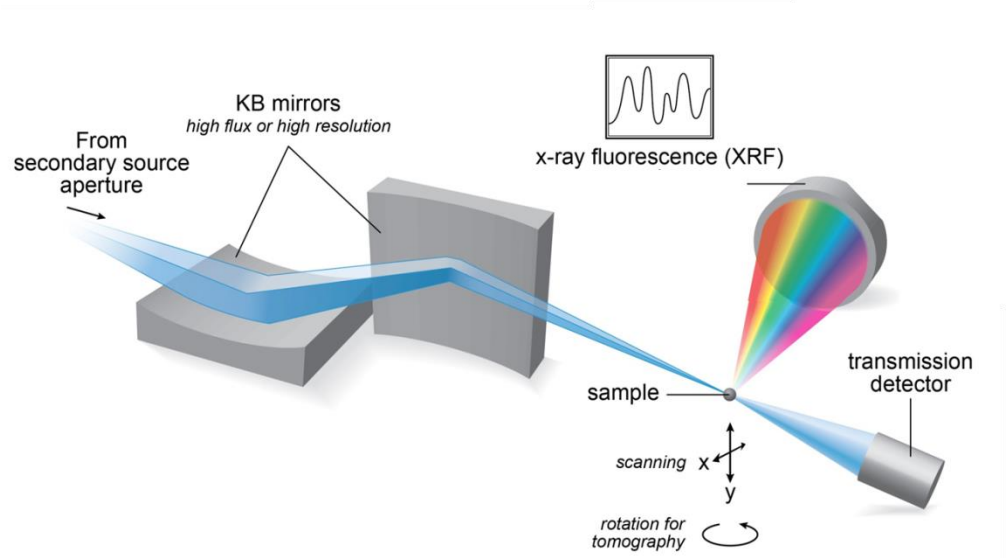

Figure S3. Schematics of x-ray fluorescence microscopy experimental setup

S2. SEM observation of the sample surface

In the Figure S4 and Figure S5, SEM images show morphology on the surface of

samples, dealloyed with different precursor composition and dealloying time. On the contrary to 3D morphology, particle size gradient didn't being characterized from surface, indicating an inhomogeneous porous structure. Therefore, conducting 3D morphological characterization becomes important in studying dealloying process.

The difference between 3D tomography and 2D surface analysis stems from unfinished dealloying process. The extent of dealloying process on the surface is closer to complete than one in the bulk. Morphology on the surface is dominantly controlled by coarsening and densification, and ligament size grow larger with longer time. It is therefore understandable that our current 3D analysis result differs from the results in SEM image and the one presented by Wada *et al.,*[1] which focuses on measuring the surface morphology by SEM.

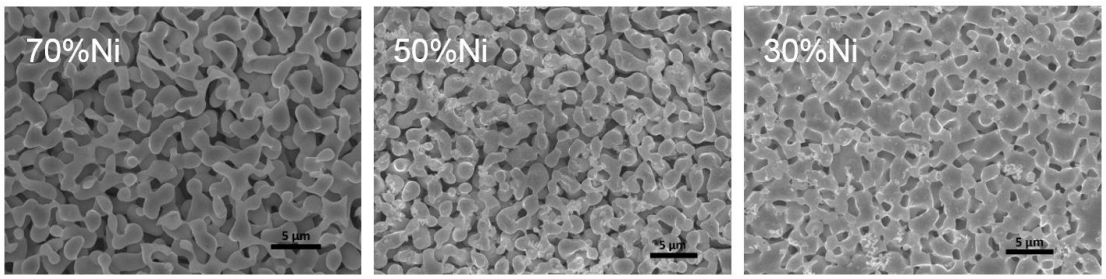

Figure S4. SEM images show surface morphology of precursor $(Fe_{0.8}Cr_{0.2})_{1-x}Ni_x$, x= 70, 50 and 30% dealloyed 10 minutes under 973K

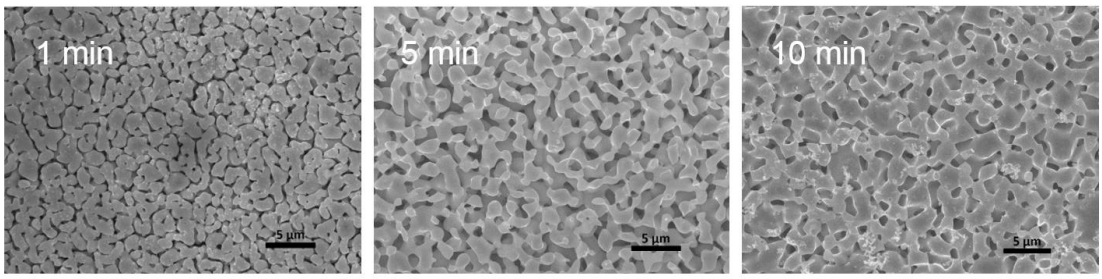

Figure S5. SEM images show precursor $(Fe_{0.8}Cr_{0.2})_{50}Ni_{50}$ dealloyed under 973K for 1 min, 5 min and 10 min

S3. Additional quantification and observation on 3D morphology

S3.1 Morphology evolution with dealloying time

Figure 2b shows np-ss dealloyed from precursor $(Fe_{0.8}Cr_{0.2})_{50}Ni_{50}$ for 1, 5 and 10 minutes, respectively. As can be seen, ligament size increases at the beginning 5 min, which result from simultaneous coarsening accompanied dealloying. Whereas little difference was found between samples dealloyed 5 min and 10 min, and this can be explained by coarsening behavior that feature size increases rate reduces over time. The quantitative analysis of average ligament size evolution with dealloying process is also shown in Figure S10. For all samples dealloyed at 1073 K, the ligament size continues increase from 5 to 10 min. It is easy to understand that the higher temperature and longer time will promote stronger coarsening and densification, causing ligaments to grow larger. In samples dealloyed at 973 K, however, the ligament size decreases by various amounts after 5 minutes. This might rise from continuous dealloying process during this entire dealloying period. The dealloyed, porous materials form larger and more stable ligaments due to their lower surface energy, caused by coarsening and densification. After 5 min dealloying, however, the effect of coarsening and densification mechanism is weaker than dealloying process. The continuous dealloying further removes Ni from the composite, reducing ligament size after 5 min. This concept of simultaneous dealloying, coarsening and perhaps densification is the key in this work to explain the morphological evolution.

Beside ligament size, Figure S6a quantitatively shows pore size distribution within each dealloying time, which displays similar trend to the ligament size

evolution. However, as seen in supplementary Figure S8, the 70% Ni samples possess a pore size increase with dealloying time, even after 5 min dealloying. This may attribute to almost no dealloying from 5 - 10 min in 50% Ni samples while dealloying continues in 70% Ni samples, which corresponds to fluorescence result.

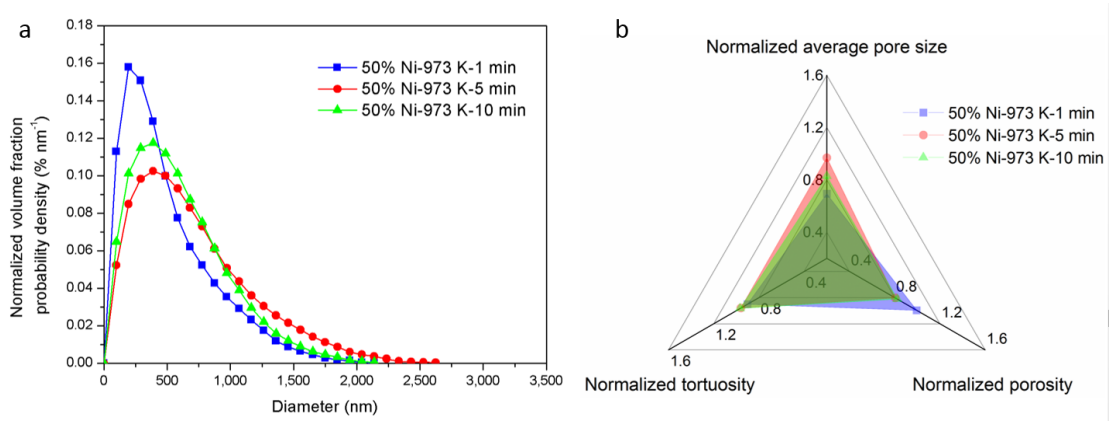

Figure S6. Structure evolution under dealloying time. (**a**) Pore size distribution with dealloying time evolution. (**b**) Normalized porosity, tortuosity and average pore size vs. each dealloying time.

S3.2 Morphology evolution with dealloying temperature

The quantitative pore size distributions of both samples $(Fe_{0.8}Cr_{0.2})_{50}Ni_{50}$ dealloyed for 10 minutes at 973 K and 1073 K are shown in Figure S7a. It shows that the 1073 K dealloying results in larger pore size, which attributes to faster coarsening of the structure at higher temperature. The morphological parameters with different dealloying temperatures are shown in Figure S7b. In contrast to the results before, the average pore size is not positively correlated to porosity and porosity slightly decreases when dealloyed at 1073 K. This demonstrates the difference in porosity is likely to attribute the densification process. Thus, to achieve ideal 3D morphology of np-ss, one should consider not only enhancing dealloying and coarsening rate, but the

influence of densification.

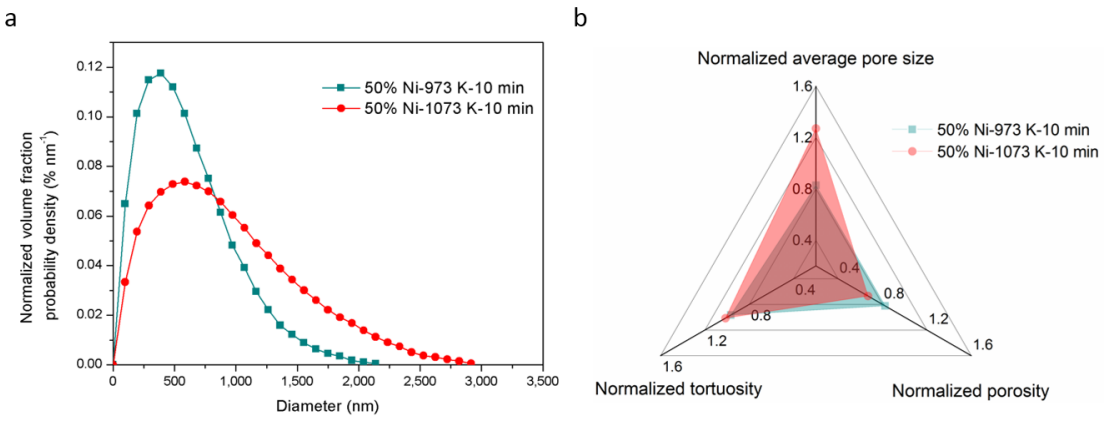

Figure S7. Morphological analysis of np-ss fabricated from precursor $(Fe_{0.8}Cr_{0.2})_{50}Ni_{50}$ dealloyed 10 minutes, at 973 K and 1073 K. (**a**) Pore size distribution with different dealloying temperatures. (**b**) Normalized porosity, tortuosity and average pore size changes with each dealloying temperature.

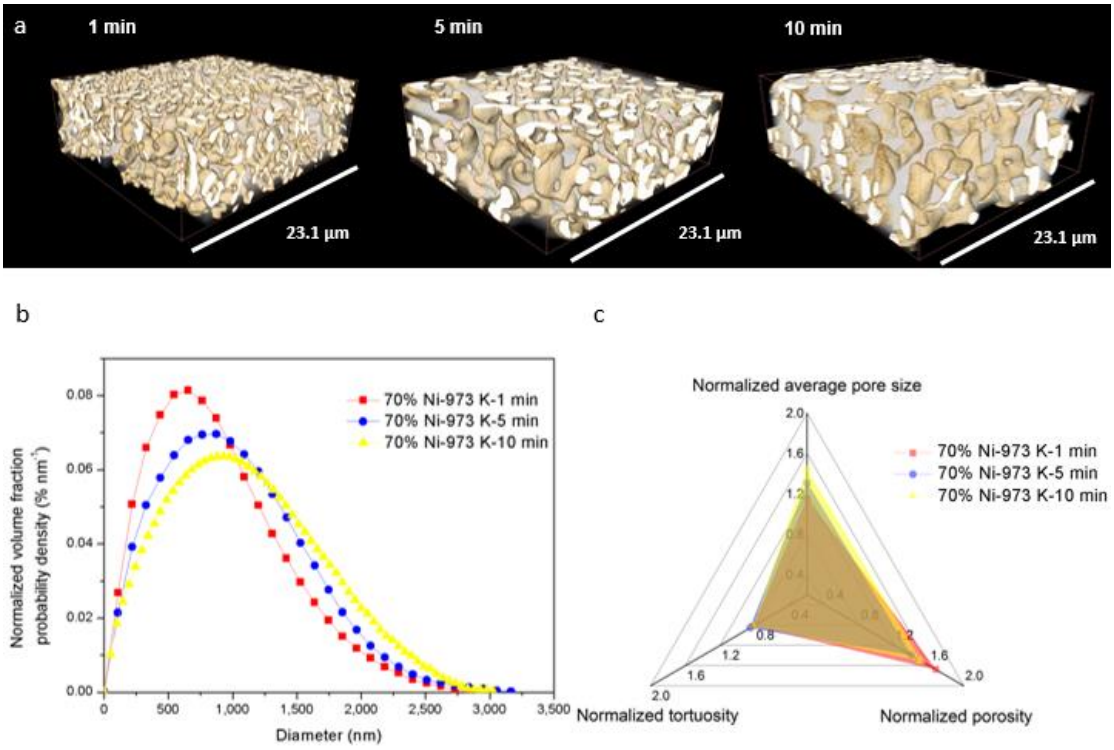

Figure S8. Volume rendering and quantitative analysis of $(Fe_{0.8}Cr_{0.2})_{30}Ni_{70}$. (**a**) 3D volume rendering of precursor $(Fe_{0.8}Cr_{0.2})_{30}Ni_{70}$ dealloyed at 973K, with 1, 5 and 10

minutes deallying time. (**b**) Pore size distribution with dealloying time evolution. (**c**) Normalized porosity, tortuosity and average pore size changes with each dealloying time.

S4. Correlation between 3D morphological properties.

While morphological properties determine the performance of the applications, the correlation between different properties also needs to be considered in an optimization process. Below we discuss this briefly.

S4.1. Average pore size with porosity

The average pore size vs. porosity evolutions is shown in the Figure S9a. Porosity is positively correlate with average pore size, the higher porosity the larger average pore size. Composition of precursor also plays the most important roles in tuning tortuosity and average pore size. Porosity is 15-20% for 30% Ni in precursor, 30-40% for 50% Ni samples and 50-70% porosity for 70% Ni samples. Average pore size distributes at 300-400 nm in diameter for 30% Ni in precursor, 500-900nm diameter for 50% Ni and 900-1200nm diameter for 70% Ni. Under the same precursor composition, higher dealloying temperature generally results in larger average pore size. To control pore size and porosity, precursor composition is also the most important dealloying condition needs to be considered.

S4.2. Average pore size and tortuosity

In the Figure S9b, we can see the inverse proportion between average pore size and tortuosity. The lower pore size, the higher tortuosity it is in the sample. Among dealloying parameters, Ni concentration in precursor plays more important role in

influencing morphology than dealloying time and temperature, which match with conclusion. Under the same precursor composition, the tortuosity does not change significantly with dealloying time and temperature. Tortuosity is around 1.1 when Ni concentration is 70%, is 1.2-1.3 at 50% Ni concentration, and is around 1.9 in 30% Ni sample. Average pore size changes with precursor composition, dealloying time and temperature. High dealloyed temperature will lead to relatively larger pore size. Therefore, to receive expect pore size and tortuosity, precursor composition is an important parameter to control.

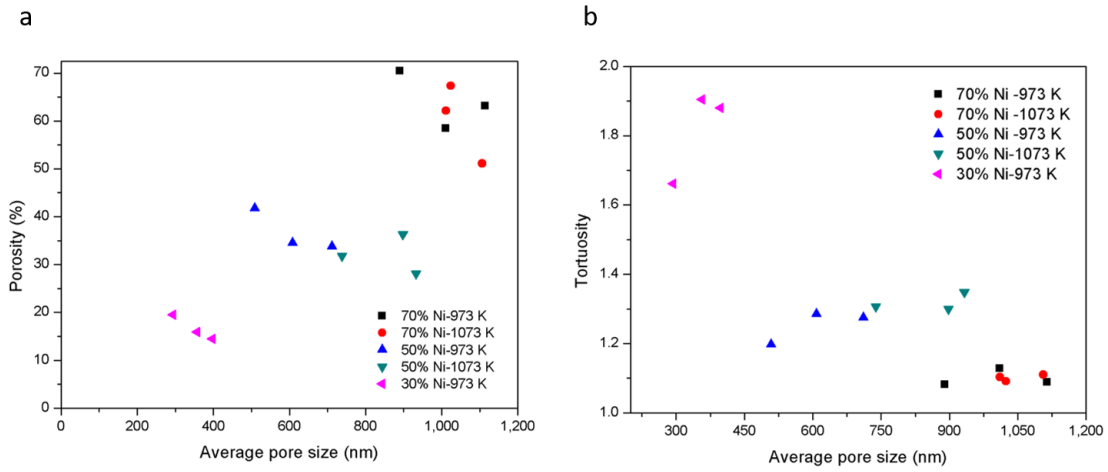

Figure S9. Correlation between 3D morphological properties. (**a**) Porosity vs. average pore size. (**b**) Tortuosity vs. average pore size

S4.3. Average pore and ligament size

In addition to pore size distribution presented, to easily compare the critical 3D properties affected by dealloying conditions, average pore size and ligament size were also calculated, shown in Figure 3d and Figure S10. respectively. Both pore and ligament sizes are determined largely by precursor composition. Comparing the size of np-ss fabricated from precursors of 30% and 70% Ni, the more Ni in precursor, the

pore size is larger, while the ligament size is smaller. Dealloying time and temperature also affect morphology; however, the trend cannot be clearly identified due to the coexisting competing mechanisms - dealloying, coarsening and densification - as described previously.

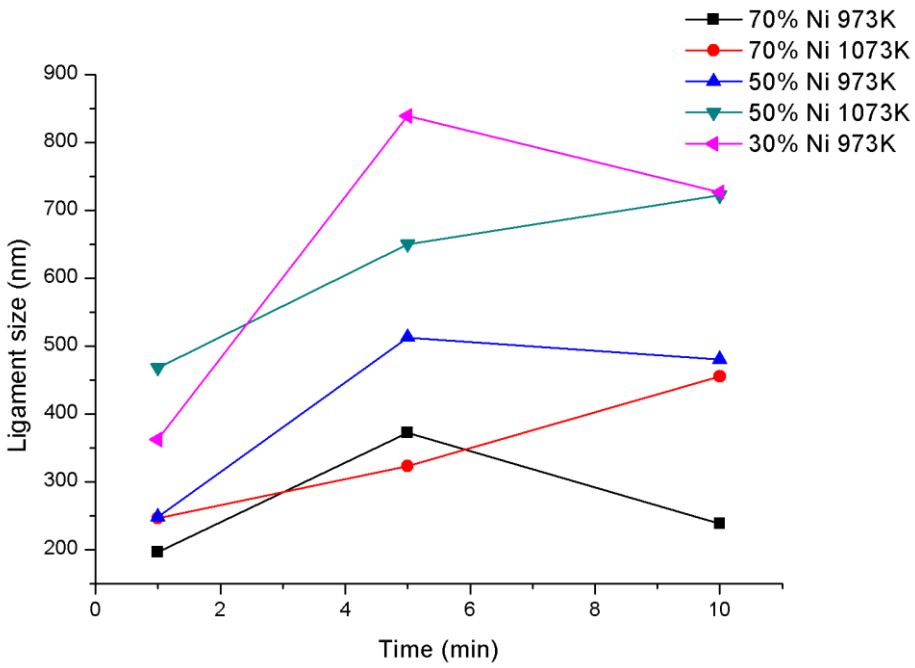

Figure S10. The ligament size evolution.

$$D = \frac{1}{Sv}$$

Where D is diameter of ligaments, S_v is specific surface area. The specific ligament surface area is defined as interface area divided by ligament volume. The calculation is based on Avizo for calculating surface area and Image J for volume size.

S4.4. Relationship between tortuosity and porosity

In addition to Bruggeman relationship, we also tested other fitting models from the

literatures for our nanoporous stainless steel sample.

The R^2 value for fitting model[2] $T(\varphi) = 1 - p \ln \varphi$ is 0.82. And for model[3] $\tau = \frac{(1+\varepsilon)^2}{\varepsilon(1+\varepsilon)^2+4\varepsilon^2(1-\varepsilon)}$, the R^2 value is 0.91.

Fitting results are plotted below.

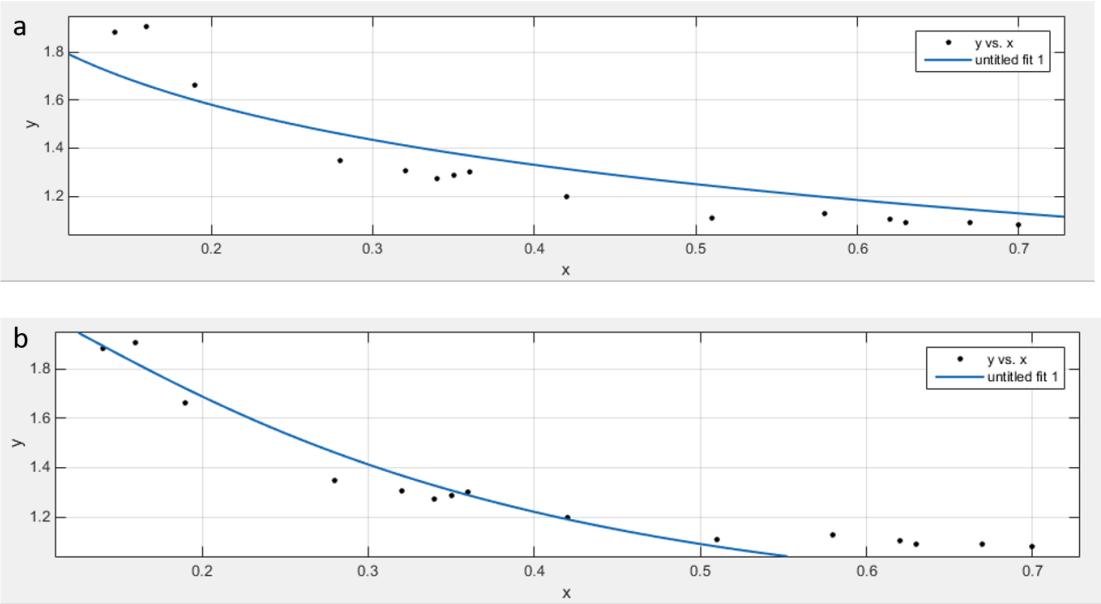

Figure S11. Fitting plot of different model. (**a**) Result of fitting model $T(\varphi) = 1 - p \ln \varphi$, with R^2 of 0.82. (**b**) Fitting result of model $\tau = \frac{(1+\varepsilon)^2}{\varepsilon(1+\varepsilon)^2+4\varepsilon^2(1-\varepsilon)}$, with R^2 of 0.91.

Therefore, comparing with other fitting model, the generalized Bruggeman relation shows best fit among the different models.

S5. Precursor XRF analysis

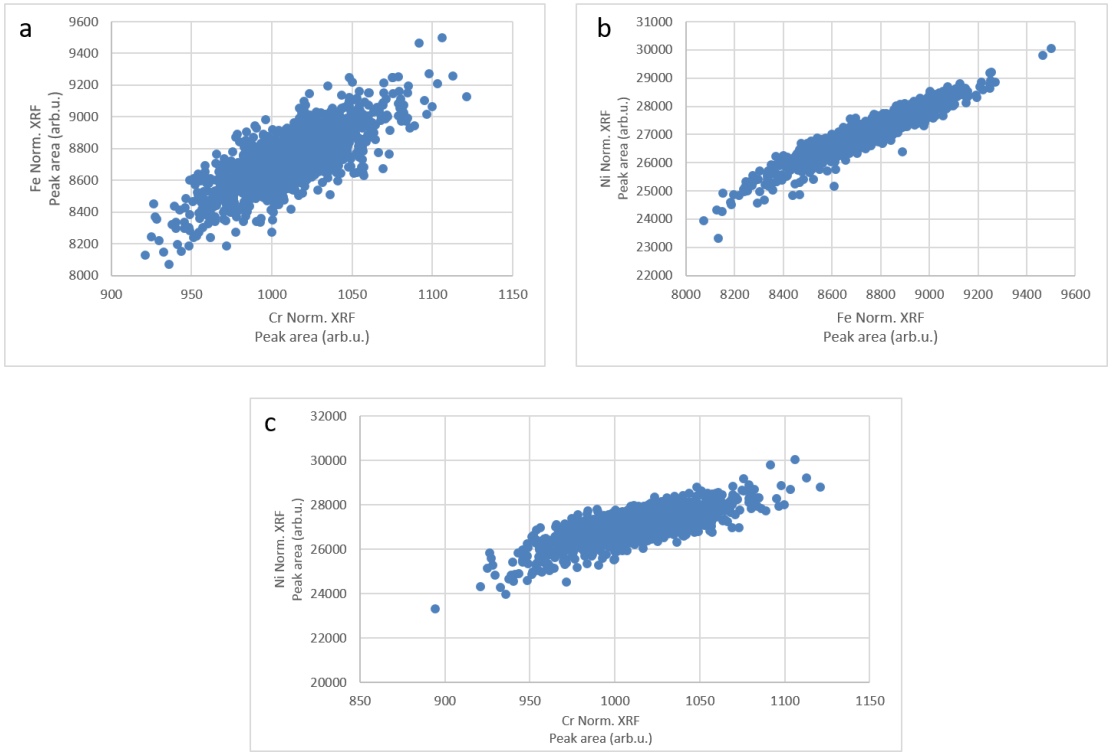

Figure S12. In the precursor $(Fe_{0.8}Cr_{0.2})_{30}Ni_{70}$, linear elemental correlation exists between (**a**) Fe/Cr, (**b**) Fe/Ni and (**c**) Cr/Ni, showing a homogeneous precursor.

S6. Anisotropic structure from dealloying

SEM images in Figure S13a shows pore size gradient along dealloying direction in np-ss. A sharp boundary, dealloying front[4] exists between dealloying region and non-dealloyed region. The pore size gradient stems from two co-existing dealloying and coarsening processes. Dealloying process removes Ni from precursor gradually, whereas coarsening, driven by minimizing surface energy, leads to growth of ligaments and/or pores. The simultaneous coarsening therefore results in a larger feature size on the surface.

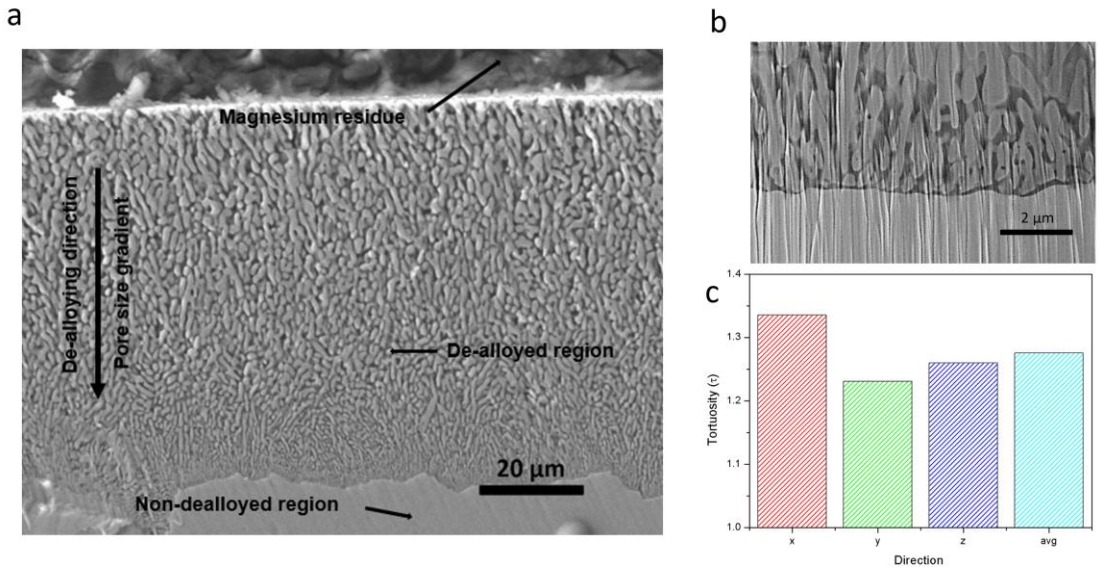

Figure S13. Inhomogeneous structure (**a**) Pore size gradient along dealloying direction shown in bulk $(Fe_{0.8}Cr_{0.2})_{50}Ni_{50}$ sample, dealloyed in 973K Mg for 5 minutes. (**b**) Gap exists between dealloying front and undealloyed region (**c**) Tortuosity along three orthogoanl axes in the sample prepared by the same processing condition in thin sample.

This anisotropy in the structure can also be validated in the 3D morphological analysis. Figure S13c shows the tortuosity along three orthogonal directions in the sample, arbitrarily defined in the x-ray nano-tomography laboratory coordinates. While it is difficult to determine which direction is precisely the dealloying direction, the anisotropic nature of this porous structure can be seen.

S7. Image processing details

S7.1. Additional details on 3D analysis

The smoothing was based on a median filter, with kernel size 3×3×3. The value of the threshold for segmentation is acquired from a histogram of image intensity, setting the minimum value between the two phases: air and steel. The fully connected network of the steel was selected using the commercial software Avizo. By alternating dilation and erosion methods, the porous structure with ligaments and pores were separated from the exterior. Porosity is calculated by pixel counting, taking the ratio between the pixel numbers of the pores and the entire sample. Each reconstruction was cut to a volume of 544 × 180 × 475 pixels (Each voxel was 48.6 × 48.6 × 48.6 nm^3, and the total size of the volume under consideration was 26.4 × 8.75 × 23.1 μm^3.) for visual comparison, but the full reconstructed images were used in the final, 3D analysis.

S7.2. Effect of surface smoothing and computing parameter on curvature analysis

Table S2 shows the parameters variation in curvature analysis. The smoothing method is selected as unconstrained smoothing. The minimal edge length is the minimal allowed edge length relative to the size of a unit grid cell in surface mesh. The smoothing extent controls the size of the filter kernel. The larger the value, the smoother the surface it is, but more fine details will lose. The nLayers determines which triangles are considered to be neighbors of a given triangle. The nAverage indicates how many times the initial curvature values computed for a triangle are

being averaged with the curvature value of direct neighbor triangles. We plot the mean curvature probability density and Gaussian curvature probability density with each parameter for comparison. As can be seen in the Figure S14, there is no difference between group 1 and 2, slight difference between group 3 and 4. The group 5, with stronger smoothing extent, shows most apparent difference among other methods, but also loses most of feature details on the surface. Therefore, we select parameter in group 1 for further analysis.

	Minimal Edge Length	Smoothing Extent	N Layers	N Average
Group 1	0	5	2	3
Group 2	0.4	5	2	3
Group 3	0	5	4	3
Group 4	0	5	2	5
Group 5	0	9	2	3

Table S2. Smoothing and computing parameters in curvature analysis.

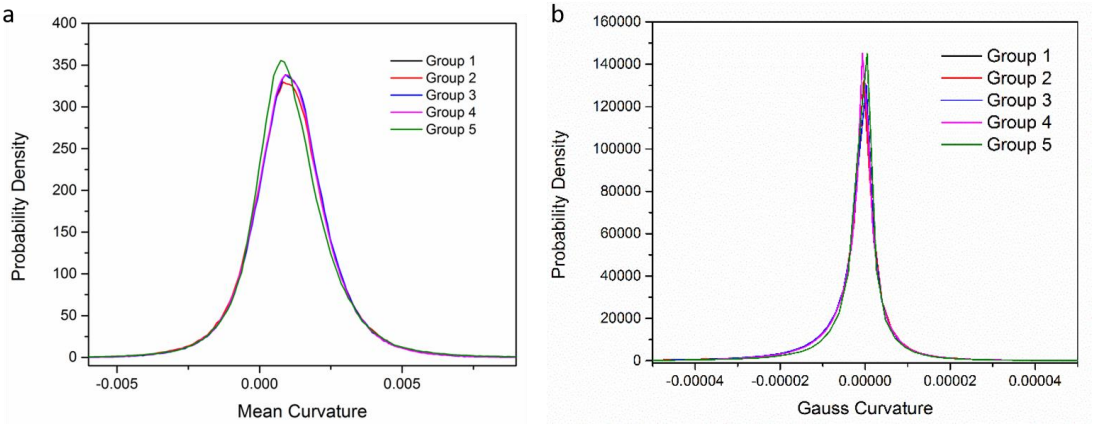

Figure S14. Probability density functions of (**a**) Mean curvature and (**b**) Gauss curvature.

S7.3. Addition discussion on ISDs

In general, an ISD has been reported to be determined by the volume fraction of the phases, as well as the mechanism of mass transport in the system.[5] The average of

mean curvature can deviate from zero when the volume fraction of the phase being quantified deviates from 50%. For a nanoporous gold sample with 50% porosity, the ISD was indeed reported to be symmetric about the zero mean curvature line (dotted line in Figure 4, where $\kappa_1 = -\kappa_2$).[6] Fujita et al. also showed that a 3D nanoporous gold structure with the 50% metal volume fraction has zero mean curvature[7]. Here, the ISDs for the 63.2% porosity (70% Ni sample) and the 15.9% porosity (30% Ni sample) shifted towards the top-right and bottom-left respectively, which are consistent with the expectation; but we observed the ISD for 34.5% porosity (50% Ni sample) shifted towards the top-right direction, which is different from the simulation case shown for a general bi-continuous system.[8] More 3D curvature analysis will further the understanding of the kinetics during the liquid metal dealloying.

S8. 3D morphological parameter effects on transport properties for potential energy storage and conversion-applications

For the work was motivated initially by potential interests in applying the materials in energy storage and conversion devices such as fuel cells and batteries, a brief discussion on the impact of the 3D morphology of np-ss on potential applications is provided below. While demonstrating the applications experimentally is beyond the scope of this current work, the discussion here may provide insights for future analysis and development. We consider how the 3D morphology of the materials may influence the properties and therefore functionalities in the contents of potential applications, mainly focusing on the transport properties.

1) **Effective diffusion coefficient:** Porosity and tortuosity directly control the

effective diffusion coefficient in porous media. The effective diffusion coefficient can be used to calculate materials transport in multiphase systems, such as PEMFC.[9] When a species diffuses in a porous media, its diffusion coefficient (D_i) can be related to its effective diffusion coefficient (D_i^{eff}) by the morphological parameters tortuosity (τ) and porosity (ε): $D_i^{eff} = \frac{\varepsilon}{\tau} D_i$. Materials with higher porosity and lower tortuosity will promote diffusion, which may be desirable to improve the PEMFC performance. The most direct way is utilizing 70% Ni as the precursor composition to achieve higher porosity and lower tortuosity. However, porosity and tortuosity, both important parameters controlling materials transport in porous structure, are not independent parameters. The quantitative relationship between the porosity and tortuosity shown in this work can provide a guideline in this respect.

2) Permeability: permeability is another important property determining the behaviour of gas and liquid flow in porous structures, critical for many applications. Determining permeability in the porous structure has been widely studied;[10-11] For instance, it has been shown that in a compacted carbon fibrous porous structure, permeability can be tuned by altering fibrous diameter and porosity.[12] Rösler, Vollertsen et al. combined thermos-mechanical processing with electrochemical dealloying, and even laser assisted techniques together, fabricating rafted porous structure with ideal permeability.[13] For the same size of the ligament structures, permeability increases with porosity. Therefore, in analogy, to achieve a higher permeability in np-ss, a higher nickel concentration in the precursor while shortening dealloying time and lowering dealloying temperature can be considered.

3) Anisotropic porous structure: the metallic melt dealloying process results in an anisotropic, directional structure with pore size gradient perpendicular the

dealloying front, as observed and quantified in this work. This pore size gradient observed in the np-ss can be a material design feature, beneficial for some applications. For instance, materials transport loss, as one of the key factors influencing fuel cells' performance,[9] previously mitigated by inserting microporous layer between gas diffusion layer and catalyst layer;[14] this approach may be replaced by an integrated gas diffusion layer with a pore size gradient. The capillary pressure on the surface of porous structure, which is the driving force for liquid water flow, can be expressed as a pressure difference between liquid P_l and gas P_g[15]: $\Delta P = P_l - P_g = \frac{2\sigma |cos\theta|}{r}$, where σ is surface tension, θ is contact angle and r is water droplet radius. Here, r can be considered as the radius of the pore. By applying a pore-size gradient structure, continuous liquid driving force can be achieved, and therefore water accumulation between each layer with different pore sizes may be reduced or eliminated. In addition, structural mismatch may exist between different layered components in PEMFCs, which will limit electrical conductivity.[16] Np-ss, as an integrated structure with size gradient can be an ideal candidate for GDL in PEMFC. Moreover, the elongation of ligaments, which is a structure with lower tortuosity, is also beneficial for materials transportation through the porous structure. This has been previously demonstrated by artificially engineered battery electrodes.[17] Here, a low-tortuosity structure can be dynamically formed during the materials synthesis. This process, driven by the thermodynamics and kinetics of materials, has advantage in material design.

Reference

1. Wada, T., Kato, H., Three-Dimensional Open-Cell Macroporous Iron, Chromium and Ferritic Stainless Steel. *Scr. Mater.* **2013,** *68* (9), 723-726.
2. Weissberg, H. L., Effective Diffusion Coefficient in Porous Media. *J. Appl. Phys.* **1963,** *34* (9), 2636-1-3.
3. Kong, W.; Zhang, Q.; Xu, X. W.; Chen, D. F., A Simple Expression for the Tortuosity of Gas Transport Paths in Solid Oxide Fuel Cells' Porous Electrodes. *Energies* **2015,** *8* (12), 13953-13959.
4. Chen-Wiegart, Y. C. K.; Wang, S.; McNulty, I.; Dunand, D. C., Effect of Ag–Au Composition and Acid Concentration on Dealloying Front Velocity and Cracking during Nanoporous Gold Formation. *Acta Mater.* **2013,** *61* (15), 5561-5570.
5. Kwon, Y.; Thornton, K.; Voorhees, P. W., Coarsening of Bicontinuous Structures via Nonconserved and Conserved Dynamics. *Phys. Rev. E* **2007,** *75* (2), 021120-1-5.
6. Chen, Y. C. K.; Chu, Y. S.; Yi, J.; McNulty, I.; Shen, Q.; Voorhees, P. W.; Dunand, D. C., Morphological and Topological Analysis of Coarsened Nanoporous Gold by X-ray Nanotomography. *Appl. Phys. Lett.* **2010,** *96* (4), 043122-1-3.
7. Fujita, T.; Qian, L. H.; Inoke, K.; Erlebacher, J.; Chen, M. W., Three-dimensional Morphology of Nanoporous Gold. *Appl. Phys. Lett.* **2008,** *92* (25), 46005-1-3.
8. Kwon, Y.; Thornton, K.; Voorhees, P. W., The Topology and Morphology of Bicontinuous Interfaces during Coarsening. *Epl* **2009,** *86* (4), 46005-1-5.
9. Weber, A. Z.; Borup, R. L.; Darling, R. M.; Das, P. K.; Dursch, T. J.; Gu, W. B.; Harvey, D.; Kusoglu, A.; Litster, S.; Mench, M. M.; Mukundan, R.; Owejan, J. P.; Pharoah, J. G.; Secanell, M.; Zenyuk, I. V., A Critical Review of Modeling Transport Phenomena in Polymer-Electrolyte Fuel Cells. *J. Electrochem. Soc.* **2014,** *161* (12), F1254-F1299.
10. Nabovati, A.; Llewellin, E. W.; Sousa, A. C. M., A General Model for the Permeability of Fibrous Porous Media Based on Fluid Flow Simulations Using the Lattice Boltzmann Method. *Composites, Part A* **2009,** *40* (6-7), 860-869.
11. Rama, P., Liu, Y., Chen, R., Ostadi, H., Jiang, K., Zhang, X., Gao, Y., Grassini, P., Brivio, D., Determination of the Anisotropic Permeability of A Carbon Cloth Gas Diffusion Layer through X-Ray Computer Micro-Tomography and Single-Phase Lattice Boltzmann Simulation. *Int. J. Numer. Methods Fluids* **2011,** *67* (4), 518-530.
12. Nabovati, A.; Hinebaugh, J.; Bazylak, A.; Amon, C. H., Effect of Porosity Heterogeneity on the Permeability and Tortuosity of Gas Diffusion Layers in Polymer Electrolyte Membrane Fuel Cells. *J. Power Sources* **2014,** *248*, 83-90.
13. Nath, O.; Stephen, A.; Rosler, J.; Vollertsen, F., Structuring of Nanoporous Nickel-based Superalloy Membranes via Laser Etching. *J. Mater. Process. Technol.* **2009,** *209* (10), 4739-4743.
14. Nam, J. H.; Lee, K. J.; Hwang, G. S.; Kim, C. J.; Kaviany, M., Microporous Layer for Water Morphology Control in PEMFC. *Int. J. Heat Mass Transfer* **2009,** *52* (11-12), 2779 - 2791.
15. Fanchi, J. R., *Principles of Applied Reservoir Simulation*. 3 ed.; Gulf Professional

Publishing: Houston, United States of America 2005.
16. Swamy, T.; Kumbur, E. C.; Mench, M. M., Characterization of Interfacial Structure in PEFCs: Water Storage and Contact Resistance Model. *J. Electrochem. Soc.* **2010,** *157* (1), B77-B85.
17. Bae, C. J.; Erdonmez, C. K.; Halloran, J. W.; Chiang, Y. M., Design of Battery Electrodes with Dual-Scale Porosity to Minimize Tortuosity and Maximize Performance. *Adv. Mater.* **2013,** *25* (9), 1254-1258.